


Article

Preparation of Porous Composite Phase Na Super Ionic Conductor Adsorbent by In Situ Process for Ultrafast and Efficient Strontium Adsorption from Wastewater

Yuliang Chen ¹, Xiangbiao Yin ², Hao Fu ^{1,3}, Zheyang Lin ¹, Guangcan Ma ¹, Xinpeng Wang ^{1,*} , Qingsong Wang ⁴ and Fangqiang Chen ^{4,*}

¹ School of Resources, Environment and Materials, Guangxi University, 100 Daxue East Road, Nanning 530004, China

² School of Nuclear Science and Technology, University of South China, 28 Changsheng West Road, Hengyang 421001, China

³ School of Chemistry & Chemical Engineering, Guangxi University, Nanning 530004, China

⁴ Nuclear and Radiation Safety Center, MEE, 9 East Zhixing Road, Beijing 102400, China

* Correspondence: wangxinpeng@gxu.edu.cn (X.W.); frankcfq@126.com (F.C.)

Abstract: Strontium, the main component of radioactive nuclear wastewater, is characterized by a high fission yield and an extended half-life. It is easily absorbed by the human body, thus greatly threatening the environment and the human body. In this study, a mesoporous composite phase sodium superionic conductor (NVP@NMP) was synthesized by the droplet template method, and the rapid capture of Sr^{2+} from wastewater was achieved by constructing a nano-heterogeneous interface to increase the ion diffusion rate. NVP@NMP showed efficient and rapid removal of strontium ions in adsorption kinetics, isothermal adsorption, solution pH, and interfering ions concentration tests, especially using the equilibrium time of 2 min for strontium absorption by NVP@NMP and a maximum theoretical adsorption capacity of 361.36 mg/g. The adsorption process was spontaneous, endothermic, and feasible. At higher concentrations of other competing ions (Na, K, Ca, Mg, and Cs), the adsorbent exhibited higher selectivity towards Sr^{2+} . TEM, XPS, and XRD analyses revealed that ion exchange was the main mechanism for the NVP@NMP ultrafast adsorption of Sr^{2+} . In this research, we investigated the feasibility of ultrafast strontium capture by sodium superionic conductor structured phosphates and explained the ultrafast strontium adsorption mechanism of NASICON materials through XPS.

Keywords: NASICON; ultrafast adsorption; strontium; ion exchange; wastewater



Citation: Chen, Y.; Yin, X.; Fu, H.; Lin, Z.; Ma, G.; Wang, X.; Wang, Q.; Chen, F. Preparation of Porous Composite Phase Na Super Ionic Conductor Adsorbent by In Situ Process for Ultrafast and Efficient Strontium Adsorption from Wastewater. *Metals* **2023**, *13*, 677. <https://doi.org/10.3390/met13040677>

Academic Editor: Jean François Blais

Received: 8 March 2023

Revised: 24 March 2023

Accepted: 28 March 2023

Published: 29 March 2023



Copyright: © 2023 by the authors. Licensee MDPI, Basel, Switzerland. This article is an open access article distributed under the terms and conditions of the Creative Commons Attribution (CC BY) license (<https://creativecommons.org/licenses/by/4.0/>).

1. Introduction

With the increasing demand for energy in modern society, nuclear energy become one of the most important non-renewable energy sources worldwide [1–5]. The isotope ^{90}Sr is the product of ^{235}U nuclear fission, and it is considered one of the most dangerous radionuclides owing to its long half-life, high fission yield, and high solubility in solution [6–8]. In addition, ^{90}Sr can be easily absorbed by the human body and remains in bones [9,10], which can eventually lead to bone cancer and leukemia [11–13]. Thus, the study of the efficient removal of ^{90}Sr in a water solution environment system is crucial. To date, a variety of technologies, including adsorption [14], filtration [15], membrane separation [16], ion exchange resin [17,18], and chemical precipitation [19] methods, have been used to capture ^{90}Sr from contaminated nuclear wastewater. Among these purification methods, adsorption has attracted considerable scholarly attention owing to its low cost, simple operation, less susceptibility to secondary contamination, superior adsorption capacity, and selectivity for systems with low concentrations of the target ions [20,21]. Commercially available conventional adsorbents, such as zeolites [22], resins [23], activated carbon [24],

and minerals [25], have been used to remove ^{90}Sr . However, these adsorbents exhibit low selectivity and long equilibrium adsorption times when adsorbing ^{90}Sr from wastewater, thus making them unsuitable for removing ^{90}Sr from wastewater. Therefore, the development of new techniques and materials for the fast and effective removal of ^{90}Sr from wastewater is vital and urgent.

Recently, sodium superionic conductor (NASICON)-structured phosphates have been widely studied because of their fast Na^+ diffusion rate and good structural stability [26,27]. The composition of NASICON material can be denoted as $\text{Na}_x\text{M}_y(\text{XO}_4)_3$, where M is the transition metals (such as V, Fe, Mn, etc.), and X is S, P, Si, As. The unit structure composed of angle sharing MO_6 octahedra and PO_4 tetrahedra form a 3D framework with migration channels for easy release of Na^+ [28,29]. NaMnPO_4 (NMP), as a typical NASICON structural material, has two different phases: maricite and olivine [30]. Compared with the olivine phase, the maricite phase (M-NMP) is thermodynamically stable. However, the lack of diffusion channels in the crystal structure of M-NMP decreases the release efficiency of sodium ions. Rapid adsorption of ^{90}Sr can be effectively achieved by improving the ion release efficiency of M-NMP. NMP materials are currently being modified by reducing their particle size [31] and ion doping [32].

Herein, a NASICON material (NVP@NMP) with large contact area, good structural stability and ultra-fast adsorption kinetics was constructed by the droplet templating method. The adsorption capacity of NVP@NMP for strontium ions in solution was investigated for the first time by a series of batch experiments. Compared with other adsorbents, our designed and synthesized hierarchical porous NVP@NMP exhibited high adsorption capacity (361.36 mg/g) and remarkable adsorption kinetics (2 min) owing to its excellent crystal structural and component properties when it was used as an adsorbent for radionuclides in water. The adsorption mechanism of NVP@NMP was investigated by XRD, XPS and quantitative experiments.

2. Materials and Methods

2.1. Material and Reagents

Vanadic oxide (V_2O_5), oxalic acid dihydrate ($\text{H}_2\text{C}_2\text{O}_4 \cdot 2\text{H}_2\text{O}$), sodium carbonate (Na_2CO_3), phosphoric acid (H_3PO_4), manganese chloride tetrahydrate ($\text{Mn}(\text{CH}_3\text{COO})_2 \cdot 4\text{H}_2\text{O}$), and polyvinyl pyrrolidone (PVP) were purchased from Aladdin. Strontium nitrate, cesium nitrate, sodium nitrate, magnesium nitrate hexahydrate, potassium nitrate, and calcium nitrate anhydrous were purchased from Damao Chemical Reagent Factory. Ethanol was purchased from Sinopharm Chemical Reagent Co. (Shanghai, China). A certain concentration of strontium adsorbed solution was obtained by dissolving strontium nitrate in deionized water, and the Sr^{2+} standard solutions for atomic absorption spectrophotometer (AAS) analysis. All reagents were used without further purification.

2.2. Synthesis of $\text{Na}_3\text{V}_2\text{PO}_4 @ \text{NaMnPO}_4$ (NVP@NMP)

In detail, 0.05 mmol of V_2O_5 and 0.2 mmol of $\text{H}_2\text{C}_2\text{O}_4 \cdot 2\text{H}_2\text{O}$ were added to 25 mL of deionized water at 80 °C and stirred for one hour. After the solution was naturally cooled to room temperature, 1.5 mmol of H_3PO_4 , 0.75 mmol of Na_2CO_3 , 0.9 mmol of $\text{Mn}(\text{CH}_3\text{COO})_2 \cdot 4\text{H}_2\text{O}$, and 50 mg of PVP were added. The EtOH were added into the mixed solution in ten fractions. The resultant solution was aged at 100 °C for 24 h in an oven. Afterward, NVP@NMP (1V: 9Mn) was obtained from the precursor by preheating the membrane at 350 °C for 5 h, followed by annealing at 700 °C for 8 h in a nitrogen atmosphere at a heating rate of 5 °C/min. NVP@NMP was synthesized by varying V: Mn molar ratios. The preparation method of NVP and NMP was the same as that of V-doped NVP/NMP without $\text{Mn}(\text{CH}_3\text{COO})_2 \cdot 4\text{H}_2\text{O}$ or V_2O_5 addition.

2.3. Characterization

The composition and physical features of different V: Mn molar ratios NVMP composites were research using different techniques. The crystal information of NVP/NMP were

obtained by X-ray powder diffraction (Bruker, D8 Discover diffractometer, Germany) using Cu K α radiation (40 kV, 40 mA, $\lambda = 1.54 \text{ \AA}$) at $2\theta = 10\text{--}80^\circ$ and a speed of $5^\circ/\text{min}$. The morphological features of adsorbents were examined using scanning electron microscopy (Sigma 300, Carl Zeiss AG, Jena, Germany), and energy dispersive spectroscopy (EDS) was used to characterize morphology and element contents in the samples before and after adsorption. The zeta potential (NanoBrook Omni, Brookhaven, New York, NY, USA) of the adsorbent samples were measured at 25°C , and the samples to be tested were dispersed in aqueous solutions of different pH values at a concentration of 0.2 mg/mL . The concentration of metal ions in the solution was measured using AAS (AA-7000, Shimadzu, Japan). Transmission electron microscopy (TEM, FEI TECNAI G2 F30, FEI, USA) was used to study the microstructure composition of adsorbent. The surface chemical composition of the adsorbent was studied by X-ray photoelectron spectroscopy (XPS, ESCALAB 250XI+, Thermo Fisher Scientific, Waltham, MA, USA). The pore size distribution and adsorption characteristics of adsorbents were determined using nitrogen adsorption/desorption isotherm and a BET-surface area analyzer (Micromeritics, TriStar II 3020, Norcross, GA, USA).

2.4. Batch Adsorption Experiments

The adsorption performance of NVP@NMP was evaluated via batch experiments. The adsorption stock solution of Sr^{2+} was obtained by dissolving $\text{Sr}(\text{NO}_3)_2$ in deionized water. Precisely, 1 mol/L of NaOH and HNO_3 solution was used to adjust the pH of the adsorption stock solution (pH value from 2 to 10). The effects of different adsorbent dosages ($0.6\text{--}1.4 \text{ g/L}$) on Sr^{2+} adsorption was determined at the initial Sr^{2+} concentration (100 ppm). The adsorption kinetic experiments were controlled with an initial solution concentration of 100 ppm , and contact times were set from 0.17 to 300 min . All adsorption experiments were performed at $\text{pH} = 3$ and room temperature (298 K) unless otherwise stated. The Effects of competitive ions on Sr^{2+} adsorption, the initial concentration of 10 ppm (0.11 mmol/L) at $\text{pH} = 3$, the concentrations of the remaining competing ions were calculated based on the ratio. The actual water adsorption, 50 mg of adsorbent was added to the water sample with an initial concentration of 10 ppm at $\text{pH} = 3$ for 10 min . The water sample were collected by Beihai Guangxi province.

The equilibrium of the NVP@NMP at the $\text{pH} = 3.0$ of the solution and at different temperatures (298 K , 308 K , 318 K) were researched.

The equilibrium adsorption amounts of Sr^{2+} were estimated as follows:

$$q_e = (C_o - C_e) \cdot V / m \quad (1)$$

where the initial concentration of Sr^{2+} was C_o (mg/L), and the initial concentration of the Sr^{2+} were $50\text{--}500 \text{ ppm}$.

The final concentration of the tested pollutants C_e (mg/L) is at equilibrium, the adsorption stock solution volume is V (L), and the mass of NVP@NMP adsorbent is m (mg).

The distribution coefficient (K_d) can be expressed as follows:

$$K_d = \frac{1000V}{m} \times \frac{C_o - C_e}{C_e} \quad (2)$$

The adsorption kinetics of NVP/NMP were discussed by pseudo-first-order kinetics, pseudo-second-order kinetics and intraparticle diffusion models; these models are given by:

$$q_t = q_e \left(1 - e^{-k_1 t} \right) \quad (3)$$

$$\frac{t}{q_t} = \frac{1}{k_2 q_e^2} + \frac{t}{q_e} \quad (4)$$

$$q_t = k_{iq} t^{1/2} + C \quad (5)$$

where the adsorption capacities at time t was qt (mg/g), the adsorbate amount at equilibrium was q_e (mg/g). The adsorption rate constants of pseudo first-and second-order kinetic models were k_1 (min^{-1}) and k_2 (g/mg/min), respectively.

The Langmuir and Freundlich equations were used to fit the Sr^{2+} at different temperatures:

$$q_e = \frac{q_{\max} \cdot b \cdot C_e}{(1 + bC_e)} \quad (6)$$

$$q_e = k_F C_e^{1/n} \quad (7)$$

where, are constants of the maximum adsorption volume was q_{\max} (mg/g), the factor of the Freundlich model were b ($\text{mg}(1-n)\text{Ln/g}$) and n .

The equilibrium constant was used to evaluate the shape of the isotherm, and it is expressed as

$$R_L = \frac{1}{1 + b C_0} \quad (8)$$

where b is the Langmuir constant, and C_0 (mg/L) is the initial concentration of adsorption. When $0 < R_L < 1$, the adsorption is favorable if $R_L = 1$ (linear), $R_L > 1$ (unfavorable), and $R_L = 0$ (irreversible).

The Gibbs free energy (ΔG^0), standard enthalpy (ΔH^0), and entropy (ΔS^0) were calculated as follows:

$$\Delta G^0 = -RT \ln K_d \quad (9)$$

$$\Delta H^0 = \Delta G^0 + T \Delta S^0 \quad (10)$$

$$\ln K_d = \Delta S^0 / R - \Delta H^0 / RT \quad (11)$$

where the gas constant (R) is 8.314 J/mol/K, and the distribution coefficient is K_d .

3. Results and Discussion

3.1. Characterization of NVP@NMP

The main synthesis process of NVP@NMP is shown in Figure S1. The mixture of NVP@NMP precursor, ethanol, and deionized water under the action of hydrogen bonds formed droplet templates. PVP enabled the precursor to maintain the stability of the mesoporous/macropore structure formed on the surface during high-temperature calcination and reduced the thermodynamically unfavorable contact area between the droplet template and the NVP@NMP precursor.

The X-ray diffraction patterns of the NVP/NMP are shown in Figure 1a. The characteristic peaks of NMP at 19.52° , 19.91° , 23.42° , 23.74° , 32.55° , 32.79° , 34.38° , and 35.07° were assigned to (020), (011), (120), (111), (220), (211), (031), and (002), respectively, which confirmed the typical M-NMP (JCPDS No. 84-0852) with the space group of Pmnb and high crystallinity [33]. With the increasing V element content, the relative crystallinity of the NVP gradually increased, which appeared at $2\theta = 14.30^\circ$, 31.59° , 32.05° , 35.74° , and 48.65° assigned to (012), (211), (116), (300), and (226), respectively. When V completely replaced Mn, a new phase was formed through crystal transformation, and the peaks at $2\theta = 14.297^\circ$, 31.589° , 32.053° , 35.743° , and 48.650° were assigned to (012), (211), (116), (300), and (226), respectively, corresponding to the NASICON-type NVP of rhombohedral space group ($R\bar{3}C$) (JCPDS. No.53-0018). The morphology information of the samples with different V-doping ratios was examined using SEM, and the results are shown in Figure 1b and Figure S2. The pores of NMP samples exhibited a macroporous/mesoporous hierarchical distribution without the addition of V. In addition, the SEM image showed that NMP exhibited a uniformly distributed hierarchical macroporous/mesoporous structure when V was not added. The N_2 adsorption-desorption isotherms were measured to obtain the detail information of BET surface and pore volumes.

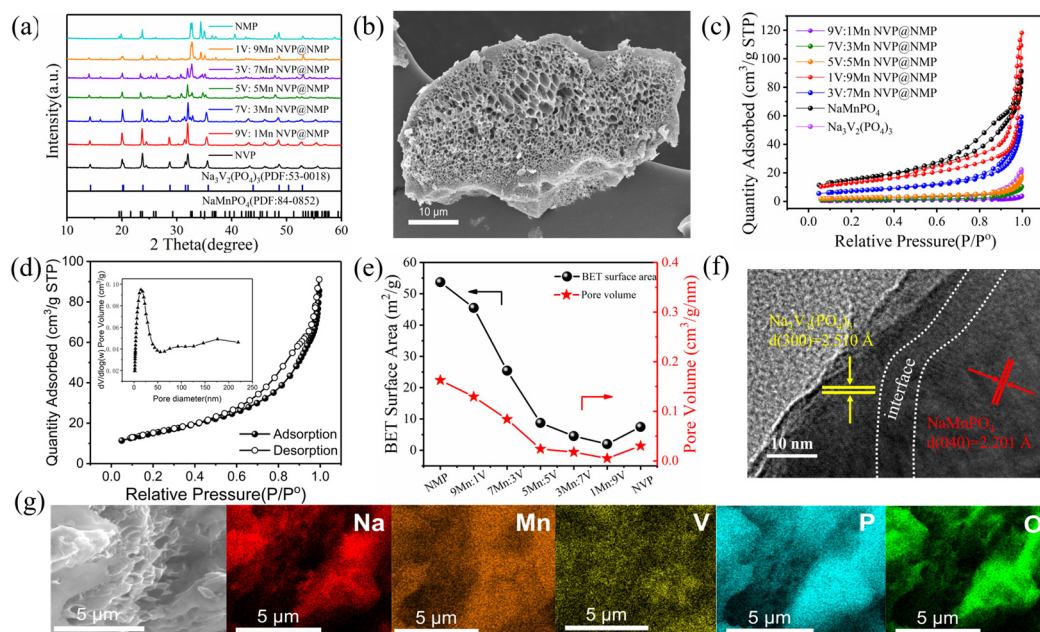


Figure 1. (a) XRD patterns of different V: Mn molar ratio adsorbents, (b) SEM image of 1V: 9Mn NVMP, (c) N_2 adsorption isotherms of different adsorbents, (d) N_2 adsorption isotherms of 1V: 9Mn (inset: pore size distribution), (e) Relationships among BET surface area, pore volume and different V: Mn molar ratio, (f) TEM image of 1V: 9Mn NVP@NMP, and (g) 1V: 9Mn NVP@NMP corresponding element mapping.

The results show (Figure 1c) that the amount of nitrogen adsorbed by the samples gradually decreases with the increase of V addition, the adsorption isotherm shows a capillary condensation step. In particular, the isotherm of 1V: 9Mn is a type-IV curve, with an H_3 hysteresis loop (Figure 1d). It is implied that 1V: 9Mn suggests the existence of macropores and mesopores, and the main pore size was estimated to be about 14.55 nm from the Barrett–Joyner–Halenda (BJH) pore size distribution. With the increase of V doping, the pore volume of the sample gradually decreased. This phenomenon is attributable to the increase in V doping, affecting the growth of NVP and NMP crystals and blocking the pores. The BET surface area and pore volume (Figure 1e) gradually decreased as the addition of V increased. The decrease in BET surface area may be attributed to the V competing with the original NMP phase after the introduction of NVP, and the pores on the surface of the sample were plugged, thus reducing the BET surface area. To understand the specific surface/interface microstructure of NVP@NMP, 1V: 9Mn was examined using TEM. As shown in Figure 1f, a clearly lattice stripe with a spacing of $\approx 2.201 \text{ \AA}$, corresponding to the NMP of (040) crystal plane, was observed on the right side. The adjacent outer layer showed lattice fringes with a spacing of $\approx 2.510 \text{ \AA}$, corresponding to the (300) plane of NVP, confirming the existence of a mixed NVP@NMP two-phase crystal structure. In addition, a nano-heterogeneous interface was observed between the primitive NMP and NVP-doped phases, which might promote the rapid diffusion of sodium ions during the adsorption process. As shown in Figure S3, the selected area electron diffraction mode of 1V: 9Mn exhibited a polycrystalline phase [34]. Furthermore, the EDS (Figures 1g and S4) revealed that 1V: 9Mn had a uniform distribution of Na, Mn, V, P, and O on the surface with an atomic ratio of 6.62: 0.8: 6.04: 7.33: 34.97.

3.2. Effects of Adsorbent Dosage and pH on Sr Adsorption

The effect of the adsorbent amount and V: Mn molar ratio on strontium adsorption onto NVP/NMP is shown in Figure 2a. The removal rate of the adsorbents increased as the adsorbent amount from 0.6 to 1.4 mg/mL. When the adsorbent amount exceeded 1.0 to 1.4 mg/mL, little change was observed in the removal of Sr^{2+} by the adsorbents (just

increase ~2%). This phenomenon is attributable to the competition of active adsorption sites resulting from the increased adsorbent concentration, thereby reducing the adsorption performance [35]. In Figure 2a, the remove rate of Sr^{2+} using the pristine NVP and NMP was low, and the removal rate of Sr^{2+} using adsorbents decreased with the increasing addition of V.

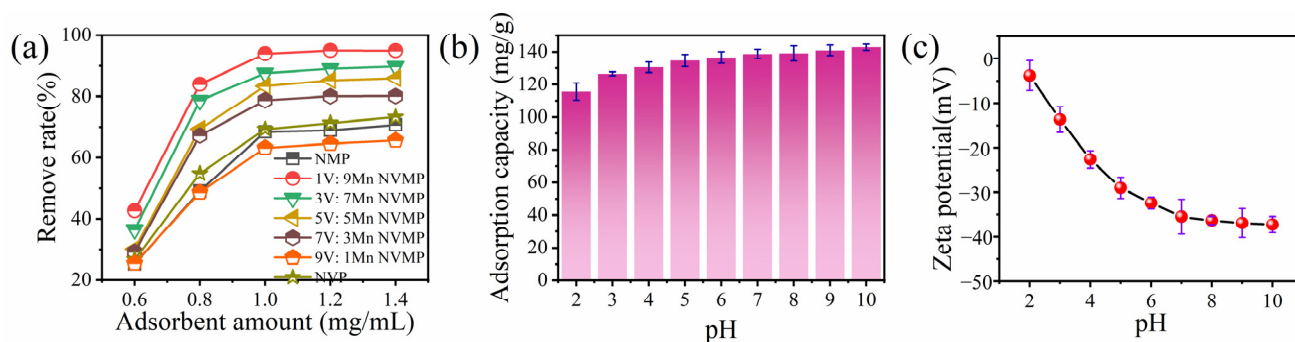


Figure 2. (a) The adsorbent dosage on the adsorption capacity of Sr^{2+} , (b) zeta potential of 1V: 9Mn at different pH values, (c) removal efficiency of Sr^{2+} with 1V: 9Mn at different pH values.

Considering that the pH of radioactive seawater could vary from acidic or alkaline, we chose a larger pH range of 2–10 to test the adsorption performance of the adsorbent under different pH conditions. The relationship between the pH value of the solution and zeta potential is shown in Figure 2b. The zeta potential results indicate a rapid decrease in the NVP@NMP surface from -3.82 mV to -37.26 mV at the same pH conditions. The negative charge forms a strong electrostatic interaction between the adsorbent and Sr^{2+} . As the pH value increases, the adsorption quantity gradually increases (Figure 2c), the adsorption capacity increases from 115.56 to the maximum of 142.78 mg/g until reaching the pH 10. This result indicates that 1 V:9 Mn has an excellent adsorption performance in the large pH range (2–10). The increase in pH of the solution reduced the protonation and enhanced the interaction between the adsorbent and the target ion, thereby increasing the adsorption performance of the adsorbent. Based on the experimental results and the adsorption environment of acidic radioactive wastewater, pH = 3 adsorbent amount is 1.0 mg/mL and 298 K were selected for further adsorption experiments.

3.3. Kinetics of Sr^{2+} Adsorption

The adsorption time between the adsorbent and the adsorbate in the solution is an important factor affecting the adsorption efficiency. The results are shown in Figure 3a, with the different molar ratios of NMP@NVP reaching the adsorption equilibrium in a short time. At 2 min, the removal rate of Sr^{2+} from the solution using 1V: 9Mn was 99%. Compared with the adsorbents at other molar ratios (Figure 3b), 1V: 9Mn exhibited an ultrafast adsorption equilibrium time.

To study the adsorption kinetics of Sr^{2+} on 1V: 9Mn, three kinetic models were selected (pseudo-first-order, second-order kinetic, and internal diffusion models) to fit the adsorption process. The fitting results (Figure 3c and Table 1) showed that the second-order kinetics had a higher degree of correlation coefficient and could better represent the adsorption process of the adsorbate at equilibrium, which means that the adsorption reaction of NVP@NMP is controlled by chemical adsorption process rather than physical adsorption process. Specifically, 1V: 9Mn had a shorter adsorption equilibrium time than other adsorbents, and the plot of t/qt vs. t showed a linear relationship (the high correlation coefficients $R^2 > 0.99$, the equilibrium adsorption of Sr^{2+} ($q_e = 102.35$ mg/g) was consistent with theoretical values ($q_{e,cal} = 101.83$ mg/g), where indicated that the adsorption process of 1V: 9Mn was chemisorption. Moreover, the rate constant of second-order kinetics was relatively high ($K_2 = 0.05$ g/mg/min) than other molar ratios, implying that the 1V: 9Mn had an ultrafast adsorption rate.

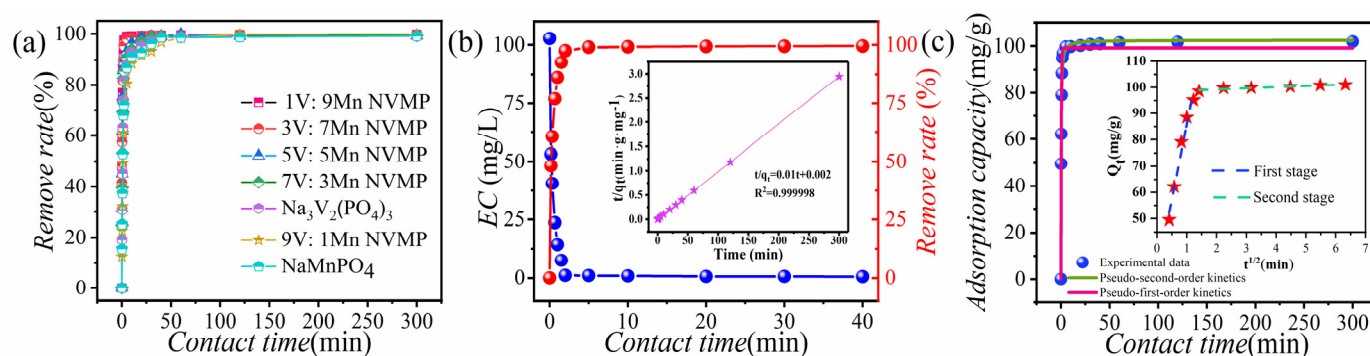


Figure 3. (a) NVP@NMP adsorption kinetic curves, (b) 1V: 9Mn adsorption kinetic curve (second-order adsorption kinetic fitting curves, EC = Equilibrium concentration), (c) Pseudo-first-order model, pseudo-second-order model and intraparticle diffusion models.

Table 1. Different NVP@NMP of the adsorption kinetic model fitting of Sr^{2+} .

Adsorbents	Pseudo-First-Order			Pseudo-Second-Order			E.T. (min)
	K_1 (L/min)	q_e	R^2	K_2 (g/mmol/min)	q_e	R^2	
1V: 9Mn	3.01	99.23	0.97	0.05	101.83	1.00	2
3V: 7Mn	2.57	98.09	0.97	0.03	102.04	0.99	5
5V: 5Mn	1.69	98.40	0.98	0.02	102.04	0.99	20
7V: 3Mn	1.34	98.20	0.98	0.02	102.14	0.99	30
9V: 1Mn	0.72	93.35	0.97	0.01	102.35	0.99	60
NVP	1.05	97.33	0.99	0.01	102.04	0.99	40
NMP	0.83	94.78	0.98	0.01	102.14	0.99	40

To understand the ultrafast kinetics of the 1V: 9Mn, the adsorption kinetic data of the 1V: 9Mn before 30 min were selected for internal diffusion model fitting. The fitting results showed two different sorption stages (Figure 3c), indicating that the adsorption process of the 1V: 9Mn was controlled with two steps [36]. The first stage was liquid film diffusion, mainly the diffusion of adsorbent from high-concentration solution to low-concentration water film. The large surface area of 1V: 9Mn provided more active sites on the surface, thereby increasing the Sr^{2+} removal rate from the solution. Because of the charge effect, Sr^{2+} in the solution was attracted to the sample surface and permeated to the adsorbent surface through the liquid film, thus increasing the adsorption process. The second stage was intraparticle diffusion. In this stage, the adsorbent diffused further from the surface to the interior through the pores. In this process, Sr^{2+} moves to the corresponding active site and exchanges ions with Na^+ . The fitted images showed that the liquid film diffusion phase of strontium occurred before 2 min, the intra-particles diffused after 2 min. None of the fitted curves of the intraparticle diffusion model passed the origin, illustrating that the adsorption process was not the only controlled by the intraparticle diffusion. Thus, the adsorption process occurred due to chemical adsorption under the synergistic effect of strong charge effect and intraparticle diffusion [37]. This excellent adsorption equilibrium time can be attributed to the following reasons: (i) the porous structure and large specific surface area improve the contact efficiency between the active site and the target ions on the adsorbent surface. (ii) The nano-heterogeneous interface resulting from the composite of NVP and NMP phases (Figure 2e) facilitated the diffusion of sodium ions at the interface and improved the ion exchange rate [34,38].

3.4. Effects of Concentrations and Temperature on Sr^{2+} Adsorption

Temperature can directly influence the adsorption process of pollutants [39]. To determine the saturated adsorption capacity (q_{max}) of the adsorbent, the adsorption isotherm of

different molar ratios was investigated. R^2 (>0.99) of the Langmuir model was higher than that of the Freundlich model (Figure 4a and Figure S5, Table S1). The adsorption capacity using the Langmuir model fitting (1V: 9Mn) was 198.88, 283.16, and 361.36 mg/g at 298, 308, and 318 K, respectively.

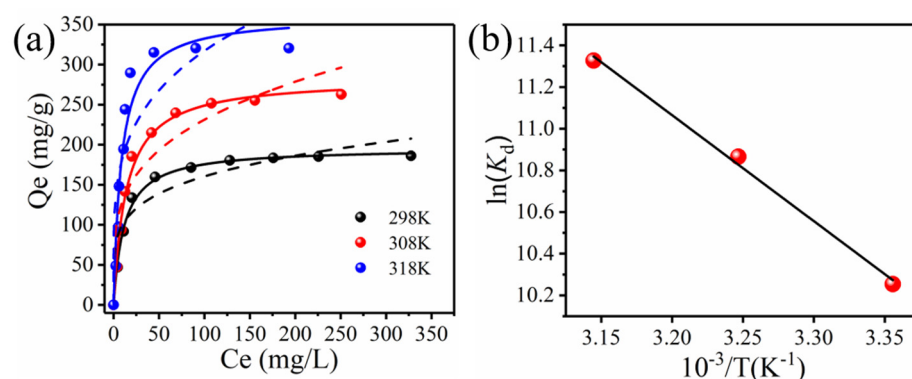


Figure 4. (a) isothermal adsorption fitting curve of Sr^{2+} adsorption using 1V: 9Mn at different temperatures and concentrations (solid lines is Langmuir model, dashed lines is Freundlich model), (b) thermodynamic investigations of 1V: 9Mn.

The equilibrium constant R_L (L/mg) in the Langmuir model can be used to confirm whether the adsorption is favorable or unfavorable [40]. The equilibrium constant (R_L) was calculated using Equation (5), and the results obtained ranged from 0.02 to 0.03, indicating that the adsorption is favorable. As shown in Table 2, both the adsorption capacity and the ultrafast adsorption kinetic equilibrium time of the adsorbent in this study were higher than most of those reported in the literature.

Table 2. Comparison of NVP/NMP with other adsorbents.

Adsorbent	pH	E.T. (min)	q_e (mg/g)	Reference
Covalent triazine framework-B	2–9	10	35.61	[41]
Metakaolin/slag-based zeolite microspheres	2–8	60	37.04	[42]
Uranyl and strontium ion-imprinted aerogel	2–7	120	160	[43]
Nano ZrO_2 - MnO_2	4–6	30	65.7	[44]
Thiacalixarene-functionalized graphene oxide	7–9	55	101.10	[45]
Layered sodium vanadosilicates	2.5–11	5	174.30	[46]
Na/Zn/Sn/S	2–12	5	32.30	[12]
Sodium manganese silicate material	2–12	1	249.00	[47]
1V: 9Mn NVMP	2–10	2	198.88	This work

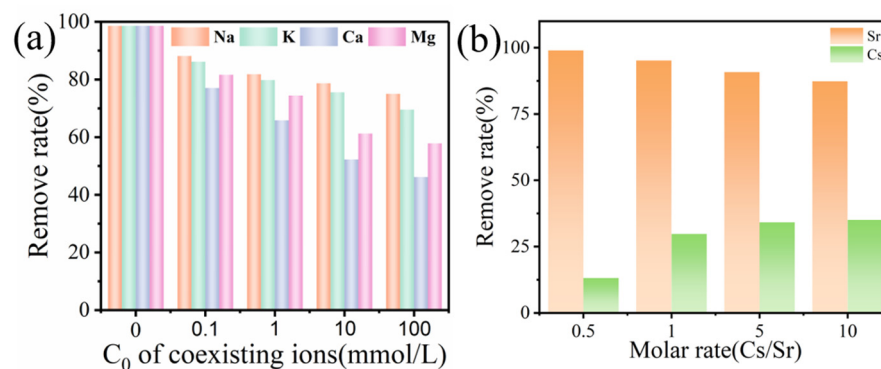
To further understand the effect of temperature, the relationship between thermodynamic parameters and reaction temperature was explored using the reaction principle of adsorbent. The results are demonstrated in Figure 4b, and the corresponding data are showed in Table 3. The negative value of ΔG° and positive value of enthalpy (ΔH° and ΔS°) indicates that adsorption is feasible and spontaneous. In addition, the values of the Gibbs free energy decreased from -25.45 to -30.00 as the temperature increased from 298 to 318 K. This result confirmed that the temperature influenced the adsorption process of strontium ions.

Table 3. Thermodynamic parameters for 1V: 9Mn NVP@NMP.

Temperature (K)	ΔH° (kJ/mol)	ΔS° (kJ/mol/K)	ΔG° (kJ/mol)
298	42.29	0.23	−25.45
308			−27.73
318			−30.00

3.5. Effects of Competitive Ions on Sr^{2+} Adsorption

Batch experiments were conducted on the adsorbent at different concentrations of competing ions to investigate the effect of competitive ions on the adsorption performance of the adsorbent. The results are shown in Figure 5a. With the increasing concentration of coexisting ions, the removal rate of Sr^{2+} gradually decreased. However, Na^+ and K^+ have a slight effect on the adsorbent; when the cation concentration is 100 mmol/L, the removal efficiency of Sr^{2+} for each is 75% and 70%, respectively. Conversely, Ca^{2+} and Mg^{2+} greatly impact the adsorbent efficiency; when the concentration is 100 mmol/L, the removal efficiency of Sr^{2+} for each is 46% and 57%, respectively.

**Figure 5.** (a) Sr^{2+} adsorption efficiency at different concentrations of competing ions, (b) Sr^{2+} adsorption efficiency at different Molar rate (Cs/Sr).

As a major element in nuclear fission, strontium separation in cesium-containing solutions facilitates resource recovery. We also investigated the selective adsorption ability of 1V: 9Mn when Cs^+ and Sr^{2+} coexist (Sr^{2+} concentration was 10 mg/L). The results (Figure 5b) show that the Cs/Sr molar ratio was 0.5, $R_{\text{Cs}} = 13.09\%$, and $R_{\text{Sr}} = 98.95\%$. Even when the Cs/Sr molar ratio was 10:1, the removal rate (87.28%) of Sr^{2+} were at high levels in acidic solutions ($\text{pH} = 3$). The above results indicate that the strontium ion capturing ability of 1V: 9Mn is less affected by competing ions and Cs^+ .

3.6. Sr^{2+} Adsorption with Actual Water

To better study the adsorption performance of the adsorbent for strontium ions in the real water environment, we spiked seawater (SW), tap water (TP), and lake water (LW). The results are shown in Figure S6. The removal rate of Sr^{2+} in different real water environments was 97.6%, 94.2%, and 91.3%. The experimental results confirm that 1V: 9Mn has a good ability to remove Sr^{2+} in the solution.

3.7. Adsorption Mechanism

To investigate the adsorption mechanism of 1V: 9Mn, the adsorption of Sr^{2+} and desorption of Na^+ were determined at the initial concentration of strontium ions (150–750 mg/L), and their quantitative relationship is shown in Figure 6a. At different adsorption temperature, the experimental data were fitted as lines (slopes near 2, $R^2 > 0.98$), meaning that 1 mol of Sr^{2+} was adsorbed when 2 mol of Na^+ was released in the solution and that Na^+ exchanged ions with Sr^{2+} .

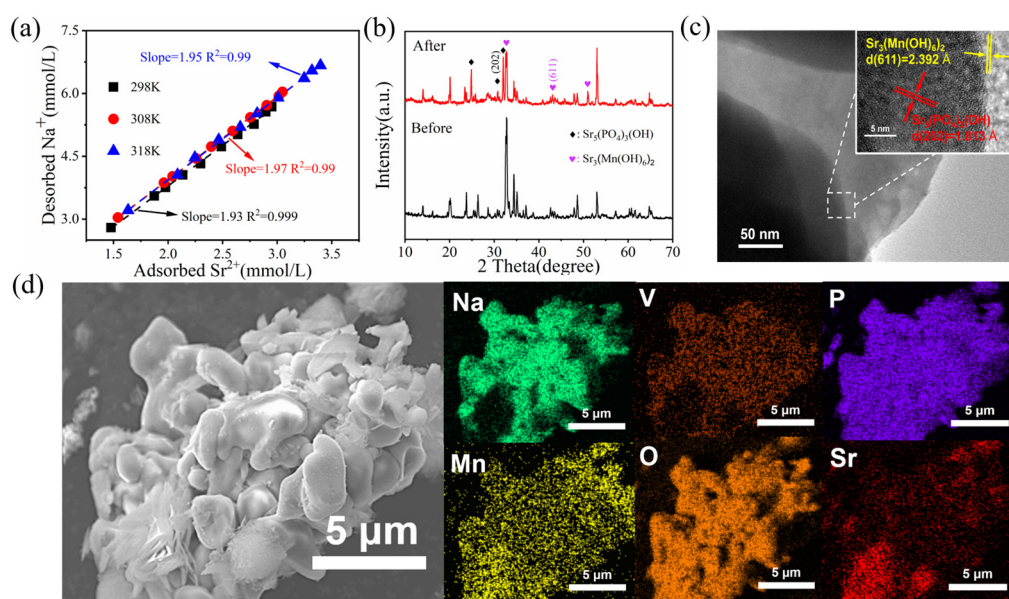


Figure 6. (a) Amount of Sr^{2+} adsorbed and Na^+ released in quantitative experiments ($m/v = 1$, $\text{pH} = 3$, $t = 30 \text{ min}$). (b) XRD patterns of adsorbent before and after adsorption; (c) TEM images of 1V: 9Mn and the enlarged images of the white regions, as indicated in the panels; (d) SEM image and the corresponding elemental (Na, V, P, O, Mn, and Sr) mapping images of the NVP@NMP (1V: 9Mn).

To investigate the crystal structure changes of NVP@NMP after the adsorption of Sr^{2+} , the changes of NVP@NMP before and after the adsorption were analyzed by SEM, XRD and TEM. The SEM image and elemental mapping of NVP@NMP after adsorption are provided in Figure 6d, which characterized the morphological changes and surface elemental distribution of NVP@NMP after strontium ion adsorption. The new crystalline material on the sample surface after adsorption can be clearly observed in Figure 6d, and the uniform elemental distribution of Sr on the NVP@NMP surface indicated that the Sr^{2+} were successfully adsorbed on the surface of the NVP@NMP. To determine the composition of the crystals precipitated on the adsorbent surface, the samples were analyzed by XRD. The XRD patterns of sample before and after adsorption are shown in Figure 6b. The peaks at 2θ of 24.89, 30.81, 32.03, 32.80, 43.11, 50.97 corresponding to $\text{Sr}_5(\text{PO}_4)_3(\text{OH})$ and $\text{Sr}_3(\text{Mn}(\text{OH})_6)_2$. The NVP@NMP samples of Sr^{2+} after adsorption was analyzed by TEM, as shown in Figure 6c, the lattice stripes of 1.81 and 2.39 \AA could be assigned to the (202) facet of $\text{Sr}_5(\text{PO}_4)_3(\text{OH})$ and the (611) facet of $\text{Sr}_3(\text{Mn}(\text{OH})_6)_2$, respectively, consistent with the XRD results. This result indicated that Sr^{2+} are immobilized on the sample surface in the form of $\text{Sr}_5(\text{PO}_4)_3(\text{OH})$ and $\text{Sr}_3(\text{Mn}(\text{OH})_6)_2$.

Subsequently, the XPS full spectrum analysis of the samples before adsorption showed in Figure 7a that the main elements contained in the samples were Na, Mn, V, P, and O, which was consistent with the results reported in the literature [41–43].

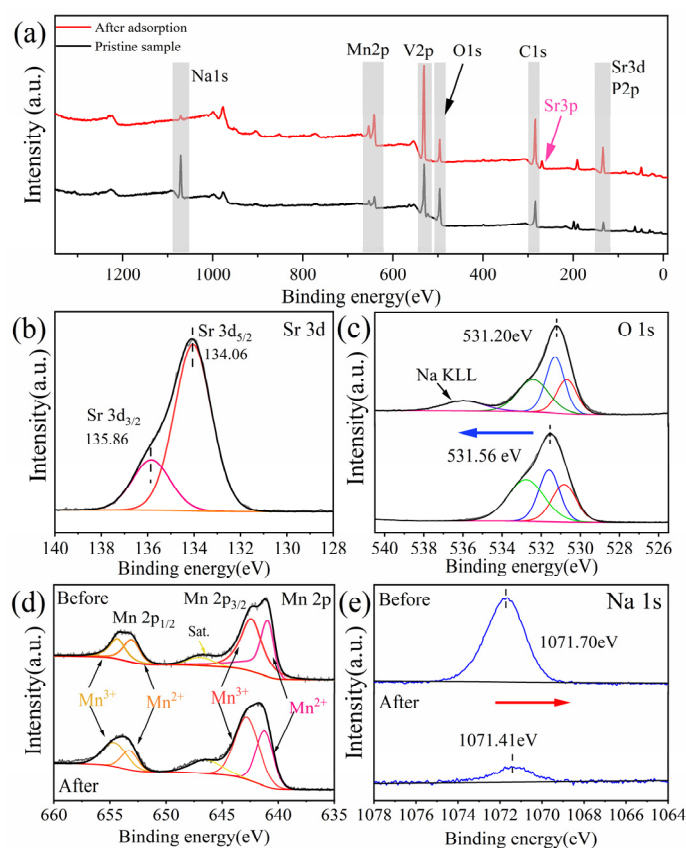


Figure 7. (a) XPS full spectrum analysis before and after Sr^{2+} adsorption by 1V: 9Mn NVP@NMP (b) High-resolution XPS spectrum analysis of Sr 3d region; (c) O 1s high-resolution XPS spectrum before and after adsorption; (d) Mn 2p region; (e) Na 1s region.

After the Sr^{2+} was adsorbed, the signal peak of Sr^{2+} appeared on the XPS spectra (Figure 7b) due to the overlap of the signal peaks of Sr3d and P2p at 133.73 eV, resulting in a significantly higher peak intensity at this location than that of the sample before adsorption. Sr3d was divided into two peaks: Sr 3d_{5/2} at 134.06 eV and Sr 3d_{3/2} at 135.86 eV, which was consistent with that in the literature report [44–46], confirming that Sr^{2+} was successfully adsorbed on the sample surface.

For the others, the O high-resolution XPS pattern (Figure 7c) was shifted to higher binding energy (from 531.20 to 531.56 eV), while the Na KLL peak disappeared, indicating that Na^+ was released into the solution during the adsorption process and exchanged ions with Sr^{2+} and that a chemical bond was formed between the adsorbed Sr^{2+} and oxygen. The high-resolution Mn 2p spectrum of 1V: 9Mn is shown in Figure 7d. Before adsorption, four fitted peaks were centered at 641, 642.5, 653.15, and 654.4 eV, indicating the presence of Mn^{2+} and Mn^{3+} in the adsorbent. After Sr^{2+} was adsorbed, the binding energy of Mn^{3+} increased (from 642.5 to 642.86 eV), indicating that the Sr^{2+} in the solution was bonded to MnO_6 . Moreover, the analysis of Na high-resolution XPS patterns (Figure 7e) revealed that the intensity of the characteristic peaks of Na1s significantly decreased before and after adsorption. Specifically, the adsorbed Na1s significantly shifted to lower binding energy (from 1072.28 to 1071.72 eV). This phenomenon was due to the release of Na^+ from NVP@NMP and exchange with Sr^{2+} [48–53].

In summary, the ultrafast adsorption mechanism of NVP/NMP (1V: 9Mn) can be described as follows (Figure 8): (1) Sr^{2+} accumulated on the adsorbent surface due to electrostatic and concentration effects. (2) When Sr^{2+} was adsorbed onto the sample surface,

sodium ions were released from the crystal structure into the solution to exchange ions with strontium ions. The ion exchange mechanism of NVP@NMP can be described as:

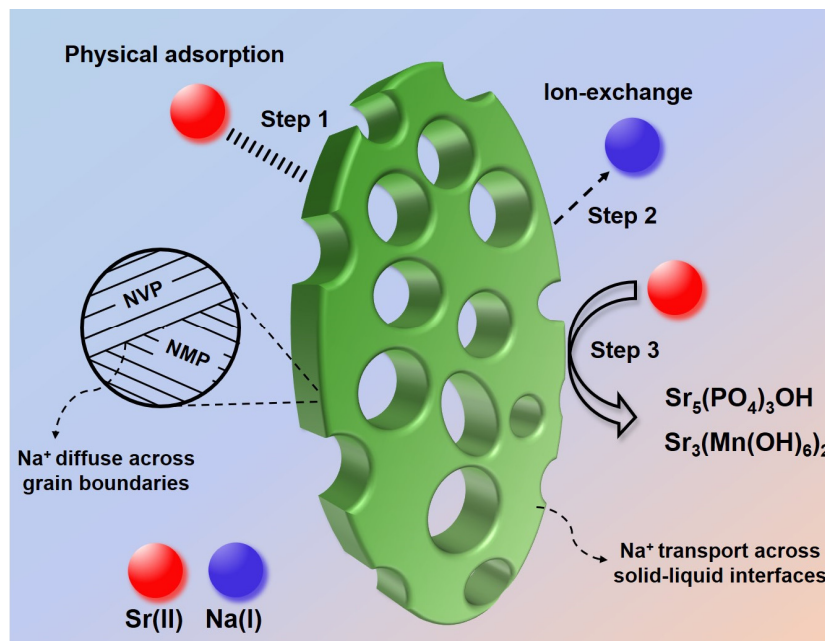


Figure 8. Mechanism of Sr^{2+} adsorption onto NVP@NMP.

After ion exchange, Sr^{2+} was bonded to PO_4 and MnO_6 in the crystal structure and then formed $\text{Sr}_5(\text{PO}_4)_3(\text{OH})$ and $\text{Sr}_3(\text{Mn}(\text{OH})_6)_2$.

4. Conclusions

In summary, we have successfully synthesized porous NVP@NMP with a nano-nonhomogeneous interfacial crystal structure through a simple polymer droplet templating strategy. The nano-nonhomogeneous interfacial crystal structure enhanced the activity of M-NMP, thus promoting the diffusion efficiency of Na^+ . NVP@NMP was used to remove Sr^{2+} from wastewater. NVP@NMP (1V: 9Mn) exhibited remarkable adsorption properties for Sr^{2+} , such as ultrafast adsorption kinetics (only 2 min), high equilibrium adsorption concentration, wide pH activity range, and strong resistance to interference. The thermodynamic analysis showed that the adsorption of Sr^{2+} on 1V: 9Mn was a spontaneous endothermic process. The adsorption isotherm curves were consistent with the Langmuir model. The adsorption experiments and XPS spectroscopy analysis showed that the adsorption mechanism of the NVP@NMP was mainly ion exchange. Compared with other adsorbents, NVP@NMP (1V: 9Mn) exhibited ultrafast removal of radioactive Sr^{2+} from wastewater.

Supplementary Materials: The following supporting information can be downloaded at: <https://www.mdpi.com/article/10.3390/met13040677/s1>, Figure S1: Preparation process of different molar ratios NVP@NMP; Figure S2: SEM image of the NVP/NMP. (a) NMP, (b) 7Mn: 3V NVP/NMP, (c) 5Mn: 5V NVP/NMP, (d) 3Mn: 7V NVP/NMP, (e) 1Mn: 9V NVP/NMP, (f) NVP; Figure S3: Selected area electron diffraction pattern of 1V: 9Mn NVP@NMP; Figure S4: The SEM-EDS spectrum of 1V: 9Mn NVP@NMP. Figure S5: Isothermal adsorption curve fitting for strontium adsorption by different molar ratios of adsorbents (solid lines is Langmuir model, dashed lines is Freundlich model). Figure S6: Efficiency of adsorbents on the removal of Sr^{2+} from solutions under different water. Table S1: Parameters calculated from the Langmuir and Freundlich models.

Author Contributions: Conceptualization, Y.C.; methodology, Y.C.; validation, G.M. and Z.L.; formal analysis, Y.C. and X.Y.; investigation, Y.C., G.M. and Z.L.; resources, X.W.; data curation, Y.C.; writing—original draft preparation, Y.C., H.F. and X.Y.; writing—review and editing, X.Y. and X.W.; visualization, X.W.; supervision, X.W., F.C. and Q.W.; project administration, X.W. and F.C.; funding acquisition, X.W. All authors have read and agreed to the published version of the manuscript.

Funding: This work was financially supported by the National Natural Science Foundation of China (21866007 and 12075066).

Institutional Review Board Statement: Not applicable.

Informed Consent Statement: Not applicable.

Data Availability Statement: The authors confirm that the findings of this study are available within the article.

Conflicts of Interest: The authors declare no conflict of interest.

References

1. Zhang, X.; Liu, Y. Nanomaterials for Radioactive Wastewater Decontamination. *Environ. Sci. Nano* **2020**, *7*, 1008–1040. [\[CrossRef\]](#)
2. Wang, K.; Wang, F.; Chen, F.; Cui, X.; Wei, Y.; Shao, L.; Yu, M. One-Pot Preparation of NaA Zeolite Microspheres for Highly Selective and Continuous Removal of Sr(II) from Aqueous Solution. *ACS Sustain. Chem. Eng.* **2019**, *7*, 2459–2470. [\[CrossRef\]](#)
3. Ishikawa, Y.; Tsukimoto, S.; Nakayama, K.S.; Asao, N. Ultrafine Sodium Titanate Nanowires with Extraordinary Sr Ion-Exchange Properties. *Nano Lett.* **2015**, *15*, 2980–2984. [\[CrossRef\]](#) [\[PubMed\]](#)
4. Wang, K.Y.; Ding, D.; Sun, M.; Cheng, L.; Wang, C. Effective and Rapid Adsorption of Sr^{2+} Ions by a Hydrated Pentasodium Cluster Templated Zinc Thiostannate. *Inorg. Chem.* **2019**, *58*, 10184–10193. [\[CrossRef\]](#)
5. Xiang, S.; Mao, H.; Geng, W.; Xu, Y.; Zhou, H. Selective Removal of Sr(II) from Saliferous Radioactive Wastewater by Capacitive Deionization. *J. Hazard. Mater.* **2022**, *431*, 128591. [\[CrossRef\]](#)
6. Almasri, D.A.; Kayvani Fard, A.; McKay, G.; Kochkodan, V.; Atieh, M.A. A Novel Adsorptive Ceramic Membrane for Efficient Strontium Removal. *J. Water Process Eng.* **2020**, *37*, 101538. [\[CrossRef\]](#)
7. Sihni, Y.; Yang, H.M.; Park, C.W.; Yoon, I.H.; Kim, I. Post-Substitution of Magnesium at CaI of Nano-Hydroxyapatite Surface for Highly Efficient and Selective Removal of Radioactive ^{90}Sr from Groundwater. *Chemosphere* **2022**, *295*, 133874. [\[CrossRef\]](#)
8. Lu, T.; Zhu, Y.; Wang, W.; Qi, Y.; Wang, A. Interconnected Superporous Adsorbent Prepared via Yeast-Based Pickering HIPEs for High-Efficiency Adsorption of Rb^+ , Cs^+ and Sr^{2+} . *Chem. Eng. J.* **2019**, *361*, 1411–1422. [\[CrossRef\]](#)
9. Alby, D.; Charnay, C.; Heran, M.; Prelot, B.; Zajac, J. Recent Developments in Nanostructured Inorganic Materials for Sorption of Cesium and Strontium: Synthesis and Shaping, Sorption Capacity, Mechanisms, and Selectivity—A Review. *J. Hazard. Mater.* **2018**, *344*, 511–530. [\[CrossRef\]](#)
10. Ding, B.; Zheng, P.; Ma, P.; Lin, J. Manganese Oxide Nanomaterials: Synthesis, Properties, and Theranostic Applications. *Adv. Mater.* **2020**, *32*, 1905823. [\[CrossRef\]](#)
11. Huo, J.; Yu, G.; Wang, J. Efficient Removal of Co(II) and Sr(II) from Aqueous Solution Using Polyvinyl Alcohol/Graphene Oxide/MnO₂ Composite as a Novel Adsorbent. *J. Hazard. Mater.* **2021**, *411*, 125117. [\[CrossRef\]](#) [\[PubMed\]](#)
12. Zhang, M.; Gu, P.; Yan, S.; Dong, L.; Zhang, G. Na/Zn/Sn/S (NaZTS): Quaternary Metal Sulfide Nanosheets for Efficient Adsorption of Radioactive Strontium Ions. *Chem. Eng. J.* **2020**, *379*, 122227. [\[CrossRef\]](#)
13. Burns, P.C.; Ewing, R.C.; Navrotsky, A. Nuclear Fuel in a Reactor Accident. *Science* **2012**, *335*, 1184–1188. [\[CrossRef\]](#)
14. Li, W.A.; Peng, Y.C.; Ma, W.; Huang, X.Y.; Feng, M.L. Rapid and Selective Removal of Cs^+ and Sr^{2+} Ions by Two Zeolite-Type Sulfides via Ion Exchange Method. *Chem. Eng. J.* **2022**, *442*, 136377. [\[CrossRef\]](#)
15. Mautner, A.; Kwaw, Y.; Weiland, K.; Mvubu, M.; Botha, A.; John, M.J.; Mtibe, A.; Siqueira, G.; Bismarck, A. Natural Fibre-Nanocellulose Composite Filters for the Removal of Heavy Metal Ions from Water. *Ind. Crop. Prod.* **2019**, *133*, 325–332. [\[CrossRef\]](#)
16. Vishwakarma, R.K.; Narayanam, P.K.; Umamaheswari, R.; Sundararajan, K. Surface Modified and Functionalized Graphene Oxide Membranes for Separation of Strontium from Aqueous Solutions. *J. Environ. Manag.* **2021**, *298*, 113443. [\[CrossRef\]](#)
17. James, A.M.; Harding, S.; Robshaw, T.; Bramall, N.; Ogden, M.D.; Dawson, R. Selective Environmental Remediation of Strontium and Cesium Using Sulfonated Hyper-Cross-Linked Polymers (SHCPs). *ACS Appl. Mater. Interfaces* **2019**, *11*, 22464–22473. [\[CrossRef\]](#)
18. Zhao, Y.M.; Cheng, L.; Wang, K.Y.; Hao, X.; Wang, J.; Zhu, J.Y.; Sun, M.; Wang, C. PH-Controlled Switch over Coadsorption and Separation for Mixed Cs^+ and Sr^{2+} by an Acid-Resistant Potassium Thioantimonate. *Adv. Funct. Mater.* **2022**, *32*, 2112717. [\[CrossRef\]](#)
19. Ullah, I.; Gloria, A.; Zhang, W.; Ullah, M.W.; Wu, B.; Li, W.; Domingos, M.; Zhang, X. Synthesis and Characterization of Sintered Sr/Fe-Modified Hydroxyapatite Bioceramics for Bone Tissue Engineering Applications. *ACS Biomater. Sci. Eng.* **2020**, *6*, 375–388. [\[CrossRef\]](#)
20. Xu, S.; Ning, S.; Wang, Y.; Wang, X.; Dong, H.; Chen, L.; Yin, X.; Fujita, T.; Wei, Y. Precise Separation and Efficient Enrichment of Palladium from Wastewater by Amino-Functionalized Silica Adsorbent. *J. Clean. Prod.* **2023**, *396*, 136479. [\[CrossRef\]](#)

21. Chen, Y.; Ning, S.; Zhong, Y.; Li, Z.; Wang, J.; Chen, L.; Yin, X.; Fujita, T.; Wei, Y. Study on Highly Efficient Separation of Zirconium from Scandium with TODGA-Modified Macroporous Silica-Polymer Based Resin. *Sep. Purif. Technol.* **2023**, *305*, 122499. [\[CrossRef\]](#)
22. Liang, J.; Li, J.; Li, X.; Liu, K.; Wu, L.; Shan, G. The Sorption Behavior of CHA-Type Zeolite for Removing Radioactive Strontium from Aqueous Solutions. *Sep. Purif. Technol.* **2020**, *230*, 115874. [\[CrossRef\]](#)
23. Singha Deb, A.K.; Manju, M.; Sengupta, A.; Ali, S.M. Efficient Separation of Strontium Ions from Aqueous Solution by Dibenzo-18-Crown-6 Functionalized Resin: Static and Dynamic Adsorption Studies with Computational DFT Insights. *Chem. Eng. J. Adv.* **2022**, *11*, 100308. [\[CrossRef\]](#)
24. Huang, T.; Zhang, S.W.; Zhou, L.; Liu, L.F. Electrokinetics Couples with the Adsorption of Activated Carbon-Supported Hydroxycarbonate Green Rust That Enhances the Removal of Sr Cations from the Stock Solution in Batch and Column. *Sep. Purif. Technol.* **2021**, *265*, 118531. [\[CrossRef\]](#)
25. Milcent, T.; Hertz, A.; Barré, Y.; Grandjean, A. Influence of the Nb Content and Microstructure of Sitinakite-Type Crystalline Silicotitanates (CSTs) on Their Sr^{2+} and Cs^+ Sorption Properties. *Chem. Eng. J.* **2021**, *426*, 15–19. [\[CrossRef\]](#)
26. Li, W.; Yao, Z.; Zhou, C.; Wang, X.; Xia, X.; Gu, C.; Tu, J. Boosting High-Rate Sodium Storage Performance of N-Doped Carbon-Encapsulated $\text{Na}_3\text{V}_2(\text{PO}_4)_3$ Nanoparticles Anchoring on Carbon Cloth. *Small* **2019**, *15*, 1902432. [\[CrossRef\]](#) [\[PubMed\]](#)
27. Zhou, W.; Xue, L.; Lü, X.; Gao, H.; Li, Y.; Xin, S.; Fu, G.; Cui, Z.; Zhu, Y.; Goodenough, J.B. $\text{Na}_x\text{MV}(\text{PO}_4)_3$ (M = Mn, Fe, Ni) Structure and Properties for Sodium Extraction. *Nano Lett.* **2016**, *16*, 7836–7841. [\[CrossRef\]](#) [\[PubMed\]](#)
28. Rajagopalan, R.; Zhang, Z.; Tang, Y.; Jia, C.; Ji, X.; Wang, H. Understanding Crystal Structures, Ion Diffusion Mechanisms and Sodium Storage Behaviors of NASICON Materials. *Energy Storage Mater.* **2021**, *34*, 171–193. [\[CrossRef\]](#)
29. Chen, M.; Hua, W.; Xiao, J.; Cortie, D.; Guo, X.; Wang, E.; Gu, Q.; Hu, Z.; Indris, S.; Wang, X.L.; et al. Development and Investigation of a NASICON-Type High-Voltage Cathode Material for High-Power Sodium-Ion Batteries. *Angew. Chem.-Int. Ed.* **2020**, *59*, 2449–2456. [\[CrossRef\]](#) [\[PubMed\]](#)
30. Li, H.; Zhang, W.; Sun, K.; Guo, J.; Yuan, K.; Fu, J.; Zhang, T.; Zhang, X.; Long, H.; Zhang, Z.; et al. Manganese-Based Materials for Rechargeable Batteries beyond Lithium-Ion. *Adv. Energy Mater.* **2021**, *11*, 2100867. [\[CrossRef\]](#)
31. Chowdhury, A.; Biswas, S.; Dhar, A.; Burada, P.S.; Chandra, A. Stable Na-Ion Supercapacitor under Non-Ambient Conditions Using Maricite- NaMnPO_4 Nanoparticles. *J. Power Sources* **2021**, *516*, 230679. [\[CrossRef\]](#)
32. Zhang, W.; Wu, Y.; Xu, Z.; Li, H.; Xu, M.; Li, J.; Dai, Y.; Zong, W.; Chen, R.; He, L.; et al. Rationally Designed Sodium Chromium Vanadium Phosphate Cathodes with Multi-Electron Reaction for Fast-Charging Sodium-Ion Batteries. *Adv. Energy Mater.* **2022**, *12*, 2201065. [\[CrossRef\]](#)
33. Chowdhury, A.; Biswas, S.; Mandal, D.; Chandra, A. Facile Strategy of Using Conductive Additive Supported NaMnPO_4 Nanoparticles for Delivering High Performance Na-Ion Supercapacitors. *J. Alloys Compd.* **2022**, *902*, 163733. [\[CrossRef\]](#)
34. Liang, L.; Sun, X.; Zhang, J.; Hou, L.; Sun, J.; Liu, Y.; Wang, S.; Yuan, C. In Situ Synthesis of Hierarchical Core Double-Shell Ti-Doped $\text{LiMnPO}_4@ \text{NaTi}_2(\text{PO}_4)_3@ \text{C}/3\text{D}$ Graphene Cathode with High-Rate Capability and Long Cycle Life for Lithium-Ion Batteries. *Adv. Energy Mater.* **2019**, *9*, 1802847. [\[CrossRef\]](#)
35. Liang, L.; Sun, X.; Wu, C.; Hou, L.; Sun, J.; Zhang, X.; Yuan, C. Nasicon-Type Surface Functional Modification in Core-Shell $\text{LiNi}_{0.5}\text{Mn}_{0.3}\text{Co}_{0.2}\text{O}_2@ \text{NaTi}_2(\text{PO}_4)_3$ Cathode Enhances Its High-Voltage Cycling Stability and Rate Capacity toward Li-Ion Batteries. *ACS Appl. Mater. Interfaces* **2018**, *10*, 5498–5510. [\[CrossRef\]](#)
36. Zhang, Z.; Gu, P.; Zhang, M.; Yan, S.; Dong, L.; Zhang, G. Synthesis of a Robust Layered Metal Sulfide for Rapid and Effective Removal of Sr^{2+} from Aqueous Solutions. *Chem. Eng. J.* **2019**, *372*, 1205–1215. [\[CrossRef\]](#)
37. Zhang, T.; Chen, J.; Xiong, H.; Yuan, Z.; Zhu, Y.; Hu, B. Constructing New $\text{Fe}_3\text{O}_4@ \text{MnO}_x$ with 3D Hollow Structure for Efficient Recovery of Uranium from Simulated Seawater. *Chemosphere* **2021**, *283*, 131241. [\[CrossRef\]](#)
38. Biomass, A.; Lucaci, A.R.; Bulgariu, D.; Ahmad, I. Equilibrium and Kinetics Studies of Metal Ions Biosorption on Alginate Extracted from Marine Red Algae Biomass (*Callithamnion corymbosum* sp.). *Polymers* **2020**, *19*, 1888.
39. Liu, X.; Pang, H.; Liu, X.; Li, Q.; Zhang, N.; Mao, L.; Qiu, M.; Hu, B.; Yang, H.; Wang, X. Orderly Porous Covalent Organic Frameworks-Based Materials: Superior Adsorbents for Pollutants Removal from Aqueous Solutions. *Innovation* **2021**, *2*, 100076. [\[CrossRef\]](#)
40. Lim, A.; Chew, J.J.; Ismadji, S.; Khaerudini, D.S.; Darsono, N.; Sunarso, J. Kinetic and Equilibrium Adsorption Study of Anionic Dyes Using Oil Palm Trunk-Derived Activated Carbon. *Mater. Today Proc.* **2022**, *64*, 1627–1638. [\[CrossRef\]](#)
41. Yu, Y.; Zhou, L.; Tang, J.; Wu, P.; Feng, L.; Ge, B.; Chen, H.; Hu, J.; Song, S.; Zeng, T. Effective Removal of Co(II) and Sr(II) from Radiocative Wastes Using Covalent Triazine Frameworks: Kinetics and Isotherm Studies. *Sep. Purif. Technol.* **2021**, *277*, 119633. [\[CrossRef\]](#)
42. Lei, H.; Muhammad, Y.; Wang, K.; Yi, M.; He, C.; Wei, Y.; Fujita, T. Facile Fabrication of Metakaolin/Slag-Based Zeolite Microspheres (M/SZMs) Geopolymer for the Efficient Remediation of Cs^+ and Sr^{2+} from Aqueous Media. *J. Hazard. Mater.* **2021**, *406*, 124292. [\[CrossRef\]](#)
43. Yin, J.; Yang, S.; He, W.; Zhao, T.; Li, C.; Hua, D. Biogene-Derived Aerogels for Simultaneously Selective Adsorption of Uranium(VI) and Strontium(II) by Co-Imprinting Method. *Sep. Purif. Technol.* **2021**, *271*, 118849. [\[CrossRef\]](#)
44. Ahmadi, S.J.; Akbari, N.; Shiri-Yekta, Z.; Mashhadizadeh, M.H.; Hosseinpour, M. Removal of Strontium Ions from Nuclear Waste Using Synthesized $\text{MnO}_2\text{-ZrO}_2$ Nano-Composite by Hydrothermal Method in Supercritical Condition. *Korean J. Chem. Eng.* **2015**, *32*, 478–485. [\[CrossRef\]](#)

45. Zhang, P.; Wang, Y.; Zhang, D. Removal of Nd(III), Sr(II), and Rb(I) Ions from Aqueous Solution by Thiocalixarene-Functionalized Graphene Oxide Composite as an Adsorbent. *J. Chem. Eng. Data* **2016**, *61*, 3679–3691. [[CrossRef](#)]
46. Zhang, X.; Liu, Y. Ultrafast Removal of Radioactive Strontium Ions from Contaminated Water by Nanostructured Layered Sodium Vanadosilicate with High Adsorption Capacity and Selectivity. *J. Hazard. Mater.* **2020**, *398*, 122907. [[CrossRef](#)]
47. Shen, Z.; Yan, G.; Chen, G.; Cao, L.; Tang, X.; Sun, Y.; Liu, J.; Yang, S.; Lin, L.; Zeng, X. Preparation and Strontium Adsorption Behaviors of a New Sodium Manganese Silicate Material. *Sep. Purif. Technol.* **2022**, *290*, 120824. [[CrossRef](#)]
48. Xiong, H.; Qian, R.; Liu, Z.; Zhang, R.; Sun, G.; Guo, B.; Du, F.; Song, S.; Qiao, Z.A.; Dai, S. A Polymer-Assisted Spinodal Decomposition Strategy toward Interconnected Porous Sodium Super Ionic Conductor-Structured Polyanion-Type Materials and Their Application as a High-Power Sodium-Ion Battery Cathode. *Adv. Sci.* **2021**, *8*, 2004943. [[CrossRef](#)] [[PubMed](#)]
49. Sun, W.; Zhao, W.; Yuan, S.; Zhang, L.; Yang, Y.; Ge, P.; Ji, X. Designing Rational Interfacial Bonds for Hierarchical Mineral-Type Trogtalite with Double Carbon towards Ultra-Fast Sodium-Ions Storage Properties. *Adv. Funct. Mater.* **2021**, *31*, 2100156. [[CrossRef](#)]
50. Sun, S.; Chen, Y.; Cheng, J.; Tian, Z.; Wang, C.; Wu, G.; Liu, C.; Wang, Y.; Guo, L. Constructing Dimensional Gradient Structure of $\text{Na}_3\text{V}_2(\text{PO}_4)_3/\text{C@CNTs-WC}$ by Wolfram Substitution for Superior Sodium Storage. *Chem. Eng. J.* **2021**, *420*, 130453. [[CrossRef](#)]
51. Shin, J.; Choi, M.; Go, C.Y.; Bae, S.; Kim, K.C.; Chon, K. NaOH-Assisted H_2O_2 Post-Modification as a Novel Approach to Enhance Adsorption Capacity of Residual Coffee Waste Biochars toward Radioactive Strontium: Experimental and Theoretical Studies. *J. Hazard. Mater.* **2022**, *435*, 129081. [[CrossRef](#)] [[PubMed](#)]
52. Yang, S.; Wu, G.; Song, J.; Hu, B. Preparation of Chitosan-Based Asymmetric Electrodes by Co-Imprinting Technology for Simultaneous Electro-Adsorption of Multi-Radionuclides. *Sep. Purif. Technol.* **2022**, *297*, 121568. [[CrossRef](#)]
53. Zhang, H.; Li, C.; Chen, X.; Fu, H.; Chen, Y.; Ning, S.; Fujita, T.; Wei, Y.; Wang, X. Layered Ammonium Vanadate Nanobelt as Efficient Adsorbents for Removal of Sr^{2+} and Cs^+ from Contaminated Water. *J. Colloid Interface Sci.* **2022**, *615*, 110–123. [[CrossRef](#)] [[PubMed](#)]

Disclaimer/Publisher's Note: The statements, opinions and data contained in all publications are solely those of the individual author(s) and contributor(s) and not of MDPI and/or the editor(s). MDPI and/or the editor(s) disclaim responsibility for any injury to people or property resulting from any ideas, methods, instructions or products referred to in the content.